

PROCEEDINGS OF SPIE

SPIDigitalLibrary.org/conference-proceedings-of-spie

Evaluation of segmentation algorithms for optical coherence tomography images of ovarian tissue

Travis W. Sawyer, Photini F. S. Rice, David M. Sawyer, Jennifer W. Koevary, Jennifer K. Barton

Travis W. Sawyer, Photini F. S. Rice, David M. Sawyer, Jennifer W. Koevary, Jennifer K. Barton, "Evaluation of segmentation algorithms for optical coherence tomography images of ovarian tissue," Proc. SPIE 10472, Diagnosis and Treatment of Diseases in the Breast and Reproductive System IV, 1047204 (7 February 2018); doi: 10.1117/12.2283375

SPIE.

Event: SPIE BiOS, 2018, San Francisco, California, United States

Evaluation of segmentation algorithms for optical coherence tomography images of ovarian tissue

Travis W. Sawyer^a, Photini F. S. Rice^b, David M. Sawyer^c, Jennifer W. Koevary^b, and Jennifer K. Barton^{a,b}

^aCollege of Optical Sciences, The University of Arizona, Tucson, Arizona, USA

^bDepartment of Biomedical Engineering, The University of Arizona, Tucson, Arizona, USA

^cTucson Medical Center, Tucson, Arizona, USA

ABSTRACT

Ovarian cancer has the lowest survival rate among all gynecologic cancers due to predominantly late diagnosis. Early detection of ovarian cancer can increase 5-year survival rates from 40% up to 92%, yet no reliable early detection techniques exist. Optical coherence tomography (OCT) is an emerging technique that provides depth-resolved, high-resolution images of biological tissue in real time and demonstrates great potential for imaging of ovarian tissue. Mouse models are crucial to quantitatively assess the diagnostic potential of OCT for ovarian cancer imaging; however, due to small organ size, the ovaries must first be separated from the image background using the process of segmentation. Manual segmentation is time-intensive, as OCT yields three-dimensional data. Furthermore, speckle noise complicates OCT images, frustrating many processing techniques. While much work has investigated noise-reduction and automated segmentation for retinal OCT imaging, little has considered the application to the ovaries, which exhibit higher variance and inhomogeneity than the retina. To address these challenges, we evaluated a set of algorithms to segment OCT images of mouse ovaries. We examined five pre-processing techniques and six segmentation algorithms. While all pre-processing methods improve segmentation, Gaussian filtering is most effective, showing an improvement of $32\% \pm 1.2\%$. Of the segmentation algorithms, active contours performs best, segmenting with an accuracy of 0.948 ± 0.012 compared with manual segmentation (1.0 being identical). Nonetheless, further optimization could lead to maximizing the performance for segmenting OCT images of the ovaries.

Keywords: optical coherence tomography, image segmentation, image processing, ovarian cancer

1. INTRODUCTION

Ovarian cancer remains the deadliest gynecologic malignancy in the United States, notwithstanding coordinated efforts to improve patient outcomes. While ovarian cancer is not excessively common, the disease maintains a high mortality rate, with median five-year survival less than 45%.¹ One cause of this is the fact that ovarian cancer can grow to a large size before causing signs or symptoms, leading to a high proportion of advanced disease at the time of detection. In fact, a large majority of patients have already experienced spread of their disease to local or distant tissues at initial diagnosis, resulting in a significantly poorer prognosis.²

This nefarious pattern of disease progression has led to strong interest in the area of ovarian cancer screening, with the ultimate goal of detecting asymptomatic tumors in their early stages, thus allowing more effective treatment. Various screening modalities have been investigated to reduce the burden of the disease including physical examination, transvaginal ultrasound (TVUS), and serum tumor marker measurement (most commonly Ca-125).³ Other screening tests and multimodal protocols have also been investigated; however, at this time no routine screening is recommended in average-risk patients.⁴ As such, there remains a strong need for a high-quality, minimally invasive modality for effective detection of early-stage ovarian malignancies.

Optical coherence tomography (OCT) is an interferometric imaging technique first introduced in 1991⁵ that yields depth-resolved, high-resolution images of tissue, providing information about the tomography and microstructure. Historically, OCT has been successfully applied to biological imaging in the human eye,⁶⁻⁸ the

Send correspondence to J.K.B. E-mail: barton@email.arizona.edu, Telephone: 520.626.0314

lung,^{9,10} the esophagus,¹¹ the coronary artery,^{12,13} as well as a number of other organs including the ovaries.^{14–16} The physical principle of OCT systems is similar to that of ultrasound, except that OCT systems measure time-resolved backscattered light instead of sound waves.¹⁷ A complicating factor of OCT is the depth dependence of the system performance. Lateral resolution varies throughout the sample depth; furthermore, absorption by the tissue attenuates the signal in addition to the axial resolution degrading in deeper tissue, as a result of breaking the assumption of single-scattering of light. Ultimately, the image statistics vary as a function of depth, which can frustrate attempts at quantitative analysis. Despite these drawbacks, OCT is a widely-applied and robust approach to characterizing tissue microstructure. In particular, OCT has shown great potential for disease diagnostics and tissue classification in the ovaries by imaging a wealth of microstructural features, including the stroma, epithelium, and collagen.^{14,15,18–20}

A myriad of different image analysis techniques have recently been investigated in the scope of classifying tissue health based on OCT images. Some examples include structure and texture analysis,^{21–24} convolutional neural networks,^{13,25,26} and other machine-learning techniques.^{10,27,28} Quantitatively characterizing tissue with such techniques has shown great promise as diagnostic aids. One important step to test and evaluate different methods relies on mouse models, which are critical to provide a systematic control in which to observe biological variations. However, in the scope of ovarian OCT imaging, the mouse ovaries must first be separated from the image background due to the small organ size relative to a typical OCT system field of view. This process, known as image segmentation, allows the relevant image content to be extracted and analyzed, preventing corruption from background features. The need for segmentation is not unique to ovarian OCT imaging: segmentation is a common challenge in medical imaging;^{29,30} unfortunately, pre-existing solutions are tuned to a given application and do not translate well between imaging modalities.³¹ Segmentation can be accomplished either manually, or automatically. While accurate, manual segmentation is time-intensive, as OCT yields three-dimensional data. Also of importance, appropriate preprocessing is required to suppress noise in order to best segment the image. Much work has investigated noise-reduction and automated segmentation for retinal OCT imaging;³² however, little has considered the application to the ovaries, which exhibit higher variance and inhomogeneity than the retina. Hence, to efficiently evaluate quantitative analysis methods for ovarian OCT imaging, finding an effective approach to automatic segmentation is critical. A robust segmentation algorithm would widely inform the field of OCT imaging as the application has expanded to organs such as the esophagus,¹¹ colon,³³ and coronary artery,¹² which also could benefit from automatic segmentation. Here we evaluate a set of preprocessing techniques and segmentation algorithms for the purpose of segmenting OCT images of the ovaries.

1.1 Image Segmentation Methods

Many different approaches to segmentation have been proposed in the scope of medical image processing.^{29,31,32} These methods can be separated into different groups, depending on the underlying mathematics involved (Fig. 1). Classical segmentation techniques partition the image into non-overlapping, continuous, segments based on the value of some features, such as brightness or texture.^{34–36} Pixel classification methods are an extension of classical approaches, albeit the constraint on region continuity is relaxed. Thresholding the image based on intensity remains one of the simplest and most intuitive approach to segmentation. In this case, a histogram is created to cluster pixels according to some feature, such as pixel intensity. The thresholds are selected to partition the intensity histogram, where the pixels residing in a given partition are assigned a label for segmentation. Depending on the feature represented in the histogram, thresholding can be used to segment based on edges or regions; other methods, such as the watershed algorithm, use a combination of the two and are referred to as hybrid algorithms.³⁷

Pattern recognition algorithms can perform segmentation by identifying inherent structure in an image. These algorithms can either be supervised or unsupervised; in either case, the algorithm identifies patterns in the image, which are then used to partition the image area. Supervised approaches are first trained on a set of manually segmented images that are used as reference; examples include artificial neural networks and support vector machines (SVM).^{38,39} Unsupervised methods, also known as clustering methods, do not need training data; however, properly initializing the algorithm parameters is essential for accuracy.^{40,41} Another class of segmentation algorithms is referred to as global optimization methods, which are based on energy minimization techniques. One such example is graph cutting, where the image is represented as an adjacency graph.^{42,43} In this graph, the vertices represent pixels of an image and the weight between two vertices is the similarity between

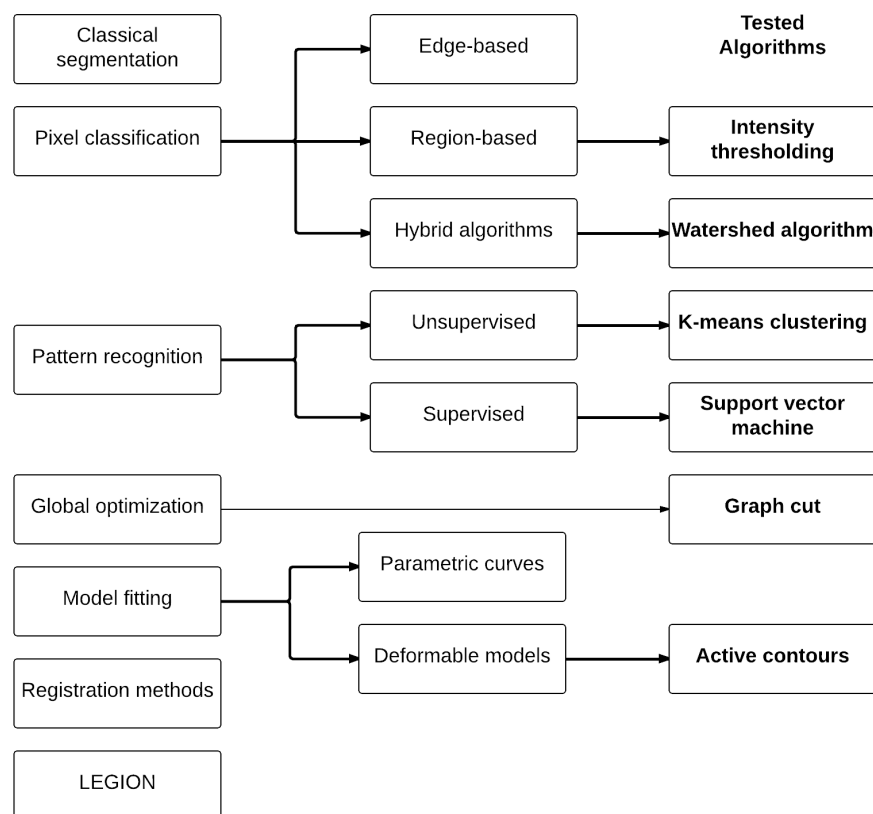


Figure 1. Image segmentation algorithms can be decomposed into different classes, depending on the mathematics. We test six of the most commonly found techniques for medical image segmentation, each of which belongs to a different class of algorithm.

two given pixels. The graph is then partitioned by cutting the vertex connections to create different groups. The optimization minimizes the summation of the weights that are cut, which can be thought of as minimizing the energy in the system. Another form of energy-minimization is to fit a model to the image, which takes advantage of morphologic or structural characteristics. Examples of this include fitting deformable models and parametric curves to an image.^{44,45} Recently, one such technique known as the active contour model has found much success in medical image segmentation.⁴⁶⁻⁴⁸ An active contour model is applied by initializing a so-called snake, which is a two-dimensional path within the image. This path can be constrained with different boundary conditions and the algorithm proceeds by fitting this path to the contours in the image. This deformable path is an energy minimizing spline influenced by image forces, defined to pull it towards object contours, which are balanced by internal forces that resist deformation. Active contours may be understood as a special case of the general technique of matching a deformable model to an image by means of energy minimization. While quite robust, the active contour approach does require knowledge of the desired contour shape beforehand to properly initialize the path.

Other classes of segmentation exist that are found less frequently in medical image analysis; for example, registration-based methods such as ATLAS warping,^{49,50} other machine learning models including artificial neural networks and active appearance modeling,^{38,51} and a method known as locally excitatory globally inhibitory oscillator network (LEGION), which is based on a biologically plausible computational framework inspired by a biological oscillator network.^{52,53} In this manuscript, we test the performance of six different segmentation techniques for segmenting OCT images of the ovaries: intensity thresholding, the watershed algorithm, k-means clustering, graph cutting, a support vector machine, and an active contour model. While numerous other approaches to segmentation exist, these six methods are a representative sample of the most widespread approaches

to segmentation in medical imaging, covering a wide range of the different classes of segmentation.

2. METHODS

2.1 OCT System

Three dimensional OCT imaging was completed with a swept source OCT system (OCS1050SS, Thorlabs). The system operates in non-contact mode with a central wavelength of 1040 nm and spectral bandwidth of 80 nm. The axial scan rate was 16 kHz and the power on the sample was measured as 0.36 mW. The system was set to average 4 axial scans. The OCT system has 11 μm transverse resolution and 9 μm axial resolution in tissue. Imaging volume was (X lateral) 4 mm \times (Y lateral) 4 mm \times (Z axial) 2 mm deep and 750 \times 752 \times 512 pixels (voxel size of approximately 5 μm \times 5 μm \times 4 μm). The image volume was exported as a series of 2D en face (X-Y) images or slices, and saved to disk as .tif image files.

2.2 Mouse Model

For this experiment, we used a mouse model of ovarian cancer, and imaged mice of different ages, genotypes and treatments. Females of the transgenic mouse model (TgMISIIR-Tag) spontaneously develop bilateral epithelial ovarian cancer.^{54,55} Both transgenic females and their wild type female littermates were imaged. Two treatment groups were investigated: those injected with Vinylcyclohexene dioxide (VCD) dissolved in sesame oil which induced follicular atresia mimicking post-menopause,⁵⁶ and those injected with vehicle (sesame oil). We imaged mice at four and eight weeks of age. In total, we acquired in a total of 70 images to analyze. By examining mice at different ages, treatments, and genotypes, we introduce biological variability into the dataset, thus creating a challenging segmentation problem.

2.3 Image Processing

2.3.1 Manual Segmentation

We established a ground truth set of segmentation masks by manually segmenting each image using the ImageJ program.⁵⁷ To do so, a given 3D image stack was loaded, where each en face slice in the stack represented a different depth. We located the first valid image by finding the most superficial image slice where the ovaries and fallopian tubes were visible and the image was not occluded by artifacts such as strong surface back reflections. A mask was then drawn around the ovaries using the Create Mask tool (Fig. 2a). The result was a binary mask where the value was one within the drawn region of interest and zero elsewhere. The image was saved to disk, and the process was repeated every ten slices until the average brightness within the ovary dropped below 20% of that recorded from the first valid image. Once this step was complete, the segmentation mask was linearly interpolated between each manually segmented slice to account for the sampling step of ten slices (Fig. 2b). We choose to segment every ten slices to reduce the time required for a full segmentation. While this action may result in a decrease in accuracy, the shape of the organs evolves roughly linearly on a small scale; thus the approximation by sampling every ten slices is reasonable. As the imaging depth increases, we expect the signal within the center of the ovaries to decrease, as incident light propagates through more volume and absorbed more. Conversely, light striking the edge of the roughly spherical ovaries will remain high, as it undergoes relatively less attenuation (Fig. 2c).

2.4 Preprocessing Techniques

Preprocessing is an essential step of OCT image analysis due to the speckle noise intrinsic to all OCT images.⁵⁸ The presence of speckle noise reduces image quality and can prohibitively frustrate some analysis techniques, such as texture analysis^{22,59} and boundary identification.³² In the body of literature, nearly all OCT image analysis methods consist of a preprocessing step to suppress electronic and speckle noise. The most common approach is to apply a median filter; however, other filtering methods have been successfully applied, which may offer advantages in preserving spatial resolution or reducing processing time.³² Of these possibilities, we examine five representative pre-processing techniques for the reduction of speckle noise in OCT images (Fig. 3). These include mean and median filtering with a 5 \times 5 pixel kernel size, as well as Gaussian filtering with a standard deviation of 5 pixels. Additionally, we applied non-linear anisotropic filtering (50 iterations; gamma=0.1) and low-pass filtering (thresholded at 50% frequency content).

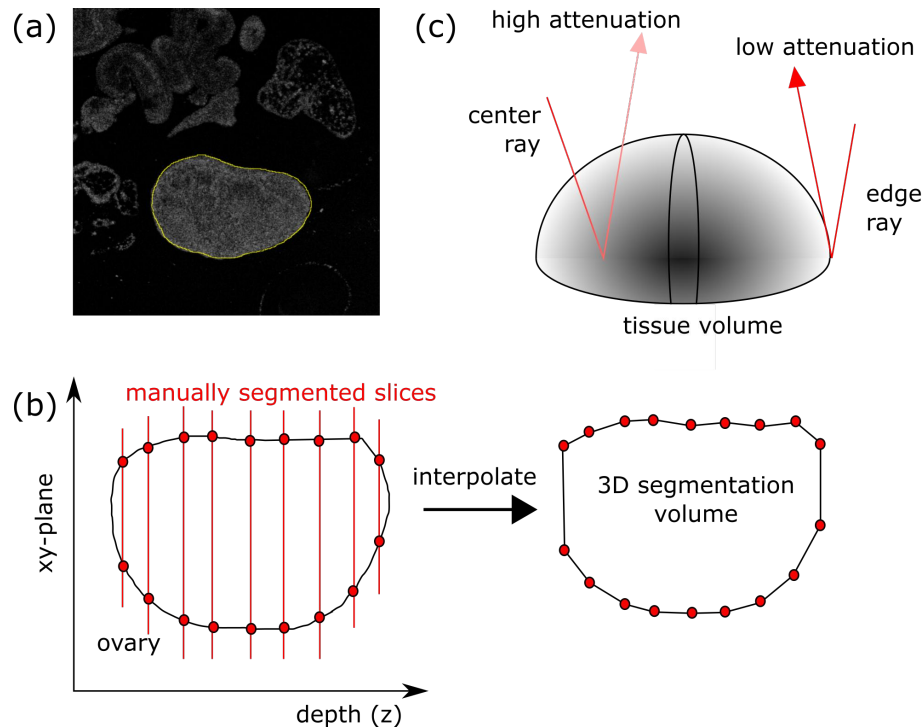


Figure 2. Individual slices of the OCT image stack were manually segmented using ImageJ (a). This was repeated throughout the image depth and interpolated to yield the final segmented volume (b). Due to the absorbing nature of tissue, as the imaging depth increases, the signal within the tissue is expected to decrease, while the signal at the edges will remain high (c).

The kernel size was selected to mitigate the effect of speckle in the image. Speckle is effectively one resolution unit in size;⁵⁸ therefore, our kernel size was chosen as two resolution units in size to eliminate the speckle. Given the system specifications, two resolution units corresponds to approximately 4.5 pixels; leading to the selection of a 5-pixel kernel size. Other noise, such as electronic noise and speckle caused by multiply scattered light will be a single pixel in size.⁵⁸ This kernel size, along with the parameters for the anisotropic diffusion filtering and low-pass filtering is consistent with what is found in the literature for applications with similar lateral resolution.^{5, 7, 60} To evaluate the performance of each preprocessing technique, we calculated the average segmentation accuracy (defined in Section 2.4.2) across a set of ten randomly selected test images for the six different segmentation approaches. We also conducted segmentation on the same set of ten test images, no preprocessing. By averaging the results of the 10 images for each preprocessing approach, and taking the ratio between the processed and unprocessed images for each segmentation approach, we compute the relative increase in performance. Since all six segmentation techniques are included, this evaluation provides insight into which filter is most appropriate for a range of segmentation approaches. We also recorded the computation time in order to compare the speed of each technique. We tested the statistical significance of the results using Analysis of Variance (ANOVA).

2.4.1 Segmentation Algorithms

We tested the performance of six different segmentation techniques: intensity thresholding, the watershed algorithm, k-means clustering, graph cutting, and a support vector machine. These six methods are a representative sample of the most widespread approaches to segmentation in medical imaging. Each belongs to a different class of algorithm and are thus indicative of how appropriate a given class may be for segmenting OCT images of the ovaries. For each case, we first filtered the images using a Gaussian filter with a standard deviation of 5 pixels to suppress speckle noise prior to segmentation, which was found to improve segmentation accuracy the most from the study in Sec. 2.4. We evaluate the accuracy of each algorithm throughout the depth of the imaging volume, investigating the maximum accuracy and processing time, as well as how well the algorithm maintains accuracy throughout the image depth. Our metric for measuring accuracy is defined in Sec. 2.4.2.

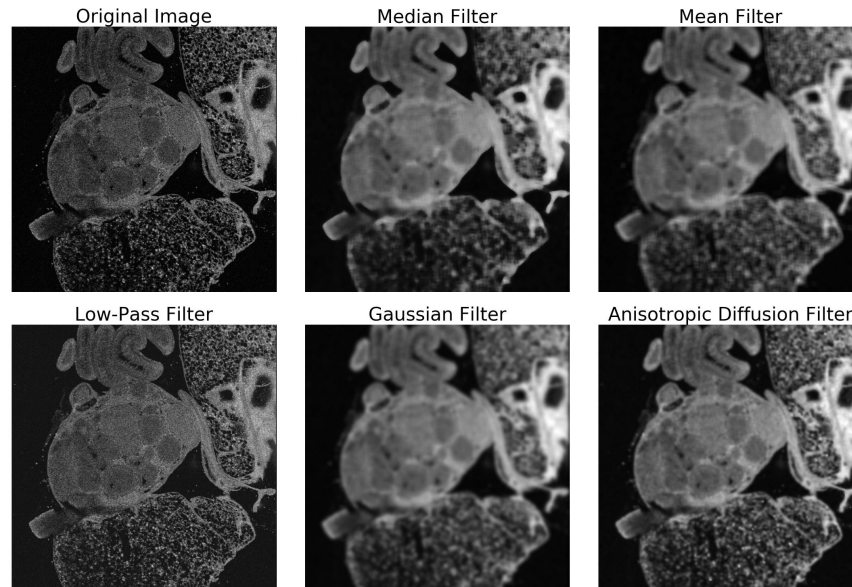


Figure 3. Five preprocessing techniques were investigated to suppress speckle noise in OCT images of the ovaries (a). We tested mean (b), median (c), low-pass (d), Gaussian (e) filters, in addition to anisotropic diffusion filtering (f). Each image here is a single en-face slice.

All image processing was completed in Python using a computer with an Intel Core I-4710HQ CPU (2.50 GHz) and 16 GB DDR3L memory. Many segmentation algorithms are readily available in Python; the algorithms tested here can be implemented using the open-source scientific computing package Anaconda. The parameters for each segmentation algorithm were determined by optimizing the performance on the most superficial image slice on a subset of ten randomly-selected images. Thresholding was performed by assigning all pixel values within a range as an organ; in this case, the threshold range was between normalized pixel values of 0.3 and 0.7.

The watershed algorithm is a region-based technique where regions of different classes are first seeded and then grown until the sources meet.⁶¹ The resulting boundary is taken as the segmentation. For this study, we generated the seeds by computing the distance transform of the image and finding the maximum value in a local 25 pixel by 25 pixel window. The watershed algorithm was then used to segment the image into nine sections, where these nine sections were ordered according to the mean pixel brightness; we then discarded the two brightest and two darkest sections and merged the remaining five into the segmentation area. The choice to discard the brightest and darkest sections was determined by iteratively testing combinations of the sections; the most accurate segmentation was given by the central five sections.

Similarly, we used k-means clustering with a compactness of 0.1 to segment into nine clusters, again where five clusters were merged to represent the ovaries using the same process as before. In this case, we constrained each of the clusters to be contiguous, ensuring that all pixels in a group were spatially connected. Next, we applied graph cutting using a normalized graph cut algorithm; first the images were pre-segmented by being clustered into thirty groups. Then, the adjacency graph was constructed and the cut made with a maximum edge value of 0.15 and a threshold of 0.05. This results in between eight to ten segmentation areas, depending on the image, which we again merged together according to the mean brightness.

We then trained a support vector machine (SVM) by splitting the image data equally into training and testing sets. For each pixel, a feature vector was constructed by applying a 15 pixel by 15 pixel median, mean and Gaussian filter ($\sigma=5$) and recording the result of each. The SVM was then trained by fitting the array of feature vectors to the ground truth manual segmentation images for each of the training set. The model was then used to predict the outcome for the test set. Following the output from the SVM, we applied a binary closing operation followed by a median filter to eliminate graininess what does graininess mean and what is an acceptable level in the result. Note that this median filter was applied to the post-processed image and is

different than the initial preprocessing filter.

Finally, we fit an active contour model to conduct the segmentation. We initialized the snake by selecting the most superficial manually-segmented image for a given image stack and using the manually-defined segmentation boundary to define the initial contour. The segmentation then proceeds throughout the image stack by using the contour from the previous image as the new seed. Thus, this approach requires a single manual segmentation, which is then propagated throughout the depth of the image to yield the full 3D segmented volume. We constrained the snake to be a closed curve, and specified two additional parameters to characterize the snake evolution: a length parameter (alpha), for which higher values make the snake contract faster and a smoothness parameter (beta). For this study, alpha was chosen as 0.001 and beta was chosen as 0.5. These values were selected by logarithmically evaluating the parameter space and selecting those values which produced the highest accuracy.

2.4.2 Performance Metric

To evaluate the performance of a given segmentation method, the resulting segmentation mask was compared to a ground truth mask obtained by manually segmenting an image. The comparison was made between the two binary masks that were generated during segmentation, where mask has a value of one corresponding to a pixel containing an organ (ovary or fallopian tube) and a value of zero otherwise. The images therefore can be thought of as matrix of ones and zeros. The accuracy was measured by correlating the two images, which is analogous to taking the dot product. Mathematically, this is expressed as

$$M = \frac{S \cdot I}{|S||I|},$$

where M is the accuracy, S is the segmented image from the algorithm and I is the ground truth image. Scaling down by the magnitude (summation of all pixels) of each image results in a value between one and zero, where one indicates that the images are identical. One implication of using this metric is that the weight associated with a true-positive result (correctly classifying an organ) is higher than that of a true negative (correctly classifying the background). Other performance metrics exist and can be used interchangeably; in this study we confine ourselves to this definition for M , which is computationally light and provides an intuitive measure of image similarity.

3. RESULTS AND DISCUSSION

3.1 Interpolation Error

We first tested the error introduced by interpolating the segmentation mask during manual segmentation. To do so, we manually segmented an ovary using every slice in the valid region. We then compared this result to the segmented mask created by interpolating between every 5, 10 and 20 slices using the similarity metric defined in Sec. 2.4.2. We find that the two masks yield an accuracy of 97.5% for sampling every 20 slices and 98.3% for sampling every 10 slices and 98.5% for sampling every 5 slices. To compare this result to the error inherent in manual segmentation, a different individual segmented the same ovary using every slice. Comparing the two complete manual segmentations yielded a similarity of 97.2%; thus, the interpolation process does not introduce more error than what is inherent to the variation in the observer. For each subsequent manual segmentation, we sampled every 10 slices.

3.2 Preprocessing Techniques

The average increase in accuracy when using different preprocessing techniques (as compared to no preprocessing), as well as the required processing time, is shown in Fig. 4. Note that the increase in accuracy is computed by segmenting a set of ten test images with each of the six segmentation algorithms. This is compared with the results when no preprocessing is applied to find the relative improvement. The results indicate that Gaussian filtering and median filtering produce the highest average improvement, with the Gaussian filtering increasing accuracy by 32% when compared to segmenting an unfiltered image. Considering processing time, the Gaussian

filtering is also most rapid, completing in an average time of 28.4 ± 1.4 ms; second is the low-pass filter with an average processing time of 73.6 ± 1.2 ms. Taking these results with the high statistical significance of the ANOVA testing ($p < 0.001$), we can conclude that Gaussian filtering is most suitable for preprocessing in our segmentation problem.

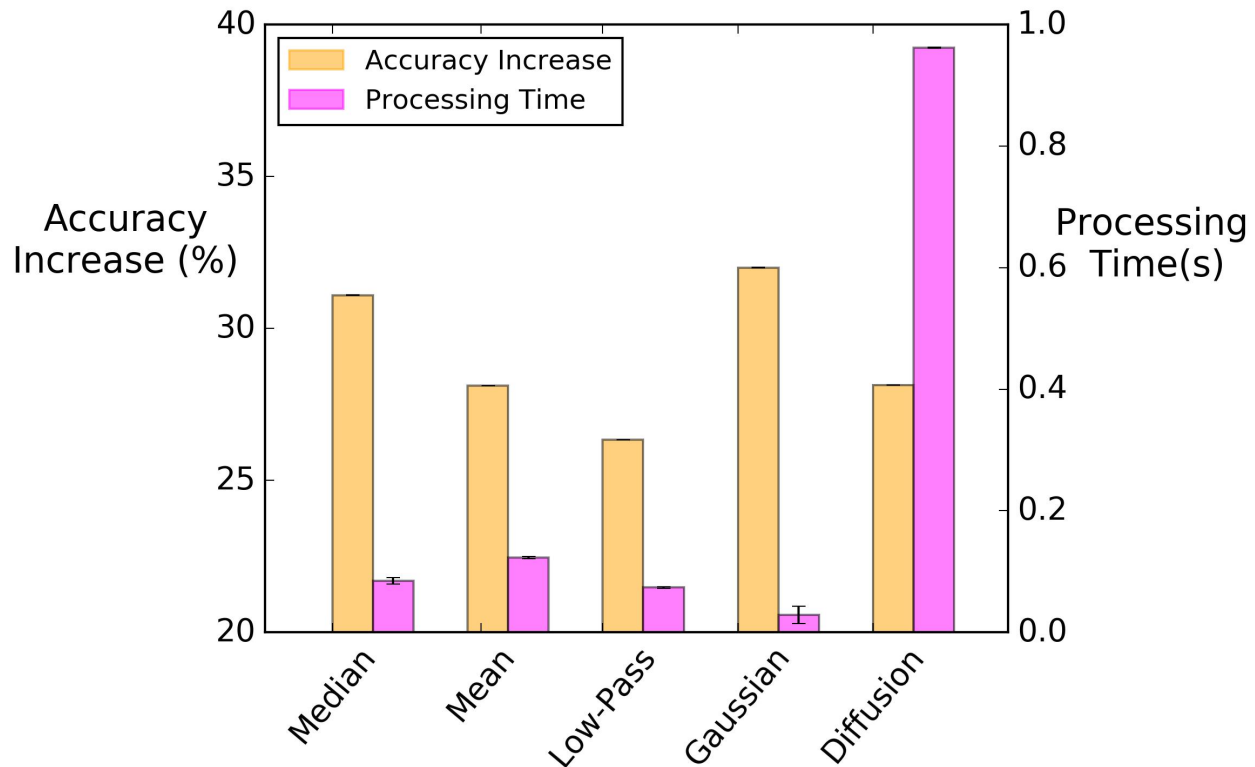


Figure 4. Average increase in segmentation accuracy (orange) and processing time (magenta) of different filtering techniques. The Gaussian filter performs best in both categories, while the median filter also exhibits high accuracy and rapid processing time.

3.3 Segmentation Algorithms

Figure 5 illustrates the results of applying the six segmentation techniques, showing the maximum segmentation accuracy throughout the image depth. While each algorithm with the exception of intensity thresholding yields high maximum accuracy (greater than 85%), the active contour method performs best, with a maximum accuracy of 0.948 ± 0.012 on average ($p < 0.01$). Evaluating the performance as a function of image depth (Fig. 6), we see that clustering and active contour modeling remain the most effective, while the other approaches suffer from high variations in accuracy throughout the depth. In particular, the watershed algorithm, SVM, and thresholding all significantly degrade in performance as a function of depth.

While clustering and graph cutting perform reasonably well, active contour modeling is most accurate. These results may be due to the high inhomogeneity of the image content for OCT images. Methods such as thresholding and the SVM classifier depend solely on pixel brightness; these vary throughout the image depth and across the area of the ovary due to non-uniform attenuation of light in the roughly spherical ovary; furthermore, much of the connective tissue has similar levels of brightness to the ovaries. Thus, intensity-based methods cannot discriminate well between these tissue types, nor do they adapt well to depth-dependent intensity.

Summarizing the results in Tab. 1, we report that active contour modeling is the most accurate approach to segmenting OCT images of ovarian tissue. The results are encouraging, showing that accurate segmentation can be achieved with minimal user interaction. We identify several objectives for future investigation. First,

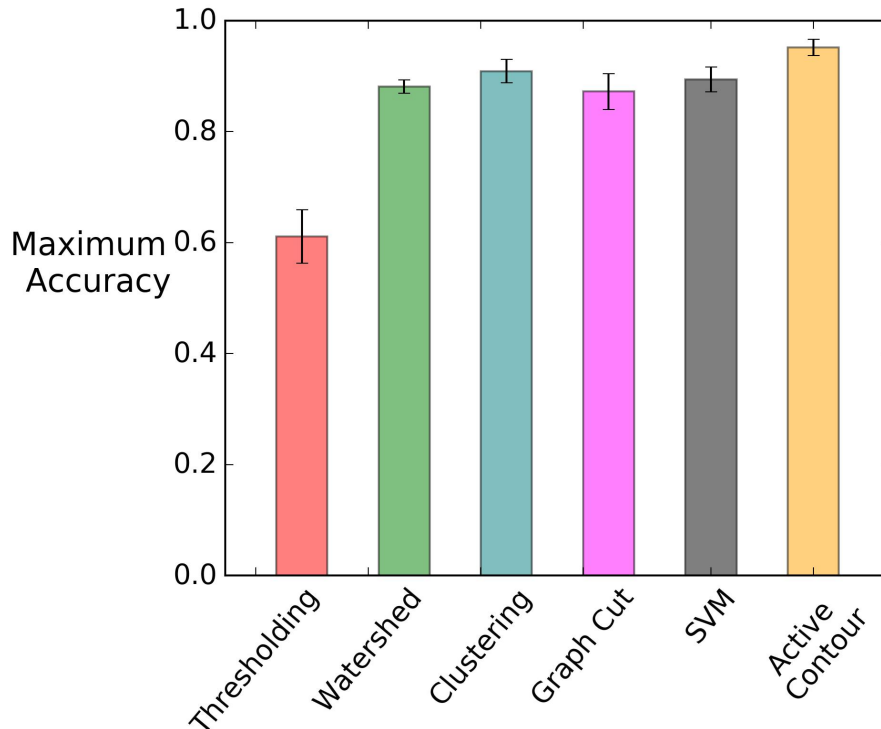


Figure 5. Maximum segmentation accuracy for each algorithm throughout the image depth. Active contour modeling performs the best, followed by K-means clustering and the support vector machine.

while we find that active contours is most effective of the tested algorithms; other segmentation approaches exist, particularly in the realm of machine learning, such as neural networks⁶² and active appearance modeling.³⁰ Machine learning continues to evolve and these algorithms could lead to more time-efficient and accurate segmentation. In addition, the feature vector used to train the SVM contains a relatively naive measure of the local image content by simply inspecting the local mean, median, and Gaussian average. Higher accuracies could be achieved by developing a more descriptive feature vector, such as one that incorporates texture analysis.⁶³ Finally, with the three-dimensionality of OCT data, traditional segmentation approaches are slow to process, as they consider each image in the stack iteratively. Extending these algorithms to apply to a three-dimensional image could both increase the accuracy while improving the processing time. While processing high dimensional data is memory-intensive, recent advances in computing have lowered this barrier, making three-dimensional processing more feasible and an exciting frontier in image processing.

Table 1. Summary of performance for each segmentation algorithm. Active contours provides both the highest maximum accuracy, as well as the most consistent accuracy throughout the depth of the tissue, as well as a rapid processing time. Note that the processing time for the SVM does not include training.

	Thresholding	Watershed	Clustering	Graph Cut	SVM	Active Contour
Maximum accuracy	0.614	0.864	0.895	0.865	0.865	0.948
Minimum accuracy	0.131	0.253	0.772	0.484	0.109	0.809
Processing Time (s)	0.001	0.289	0.954	1.638	14.16	0.274
Training Required	None	None	None	None	Training set	Single seed image

ACKNOWLEDGMENTS

We would like to thank Dr. Sarah Bohndiek and Marcel Gehrung for technical discussion and feedback. This material is based upon work supported by the National Science Foundation Graduate Research Fellowship

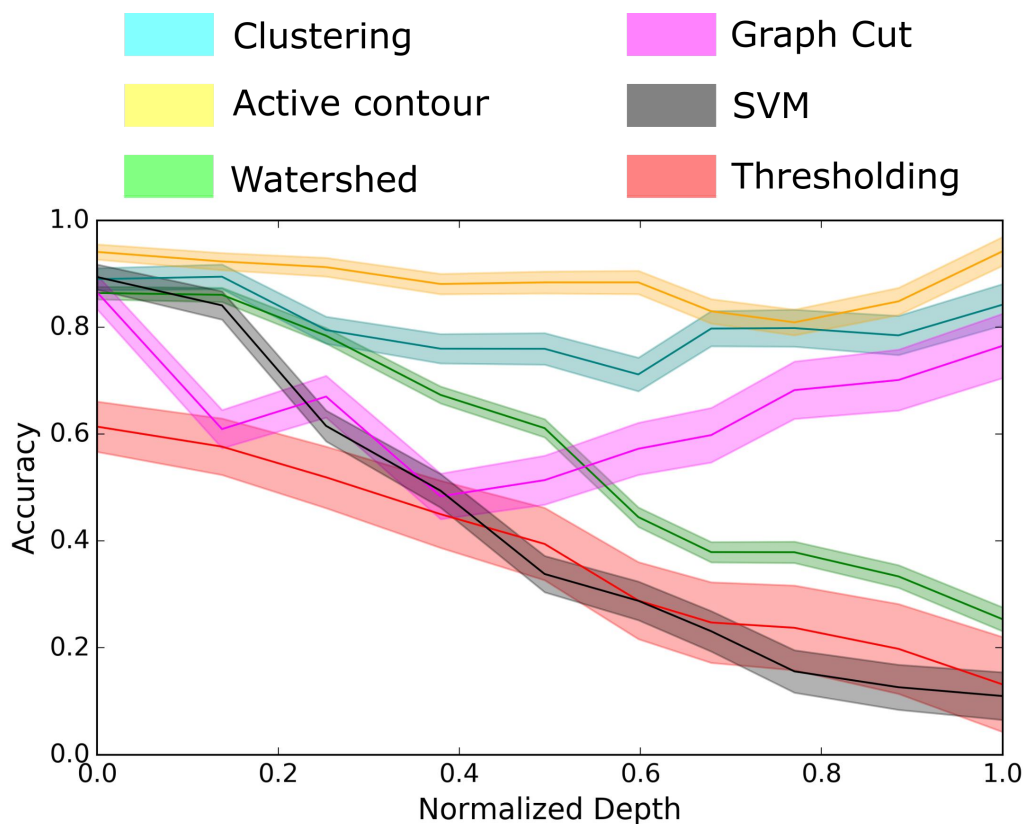


Figure 6. Segmentation accuracy as a function of image depth. The active contour model maintains high accuracy throughout the depth while thresholding, the watershed algorithm and the SVM degrade rapidly throughout the depth. Clustering and graph cutting perform reasonably well, but have a larger variation than active contours.

Program under Grant No. DGE-1143953. Any opinions, findings, and conclusions or recommendations expressed in this material are those of the author(s) and do not necessarily reflect the views of the National Science Foundation. This work was also funded by the National Institutes of Health / National Cancer Institute grant number 1R01CA195723, the University of Arizona Cancer Center, grant number 3P30CA023074.

REFERENCES

- [1] Barnholtz-Sloan, J. S., Schwartz, A. G., Qureshi, F., Jacques, S., Malone, J., and Munkarah, A. R., "Ovarian cancer: Changes in patterns at diagnosis and relative survival over the last three decades," *Am. J. Obstet. Gynecol.* **189**(4), 1120–1127 (2003).
- [2] Maringe, C., Walters, S., Butler, J., Coleman, M. P., Hacker, N., Hanna, L., Mosgaard, B. J., Nordin, A., Rosen, B., Engholm, G., Gjerstorff, M. L., Hatcher, J., Johannesen, T. B., McGahan, C. E., Meechan, D., Middleton, R., Tracey, E., Turner, D., Richards, M. A., and Rachet, B., "Stage at diagnosis and ovarian cancer survival: Evidence from the international cancer benchmarking partnership," *Gynecol. Oncol.* **127**(1), 75–82 (2012).
- [3] Carlson, K. J., "Screening for ovarian cancer," *UpToDate* (2017).
- [4] Moyer, V. A., "Screening for ovarian cancer: U.S. Preventive services task force reaffirmation recommendation statement," (2012).
- [5] Huang, D., Swanson, E., Lin, C., Schuman, J., Stinson, W., Chang, W., Hee, M., Flotte, T., Gregory, K., Puliafito, C., and et, a., "Optical coherence tomography," *Science* **254**(5035), 1178–1181 (1991).
- [6] Swanson, E. a., Izatt, J. a., Hee, M. R., Huang, D., Lin, C. P., Schuman, J. S., Puliafito, C. a., and Fujimoto, J. G., "In vivo retinal imaging by optical coherence tomography," *Opt. Lett.* **18**(21), 1864–6 (1993).

- [7] Hee, M. R., Izatt, J. A., Swanson, E. A., Huang, D., Schuman, J. S., Lin, C. P., Puliafito, C. A., and Fujimoto, J. G., "Optical coherence tomography of the human retina," *Arch. Ophthalmol.* **113**(3), 325 (1995).
- [8] Abramoff, M., Garvin, M. K., and Sonka, M., "Retinal imaging and image analysis," *IEEE Rev. Biomed. Eng.* **1**(3), 169–208 (2010).
- [9] Tsuboi, M., Hayashi, A., Ikeda, N., Honda, H., Kato, Y., Ichinose, S., and Kato, H., "Optical coherence tomography in the diagnosis of bronchial lesions," *Lung Cancer* **49**(3), 387–394 (2005).
- [10] Otte, S., Otte, C., Schlaefer, A., Wittig, L., Hüttmann, G., Dromann, D., and Zeli, A., "OCT A-Scan based lung tumor tissue classification with Bidirectional Long Short Term Memory networks," in [*Machine Learning for Signal Processing (MLSP), 2013 IEEE International Workshop on*], 1–6 (2013).
- [11] Lightdale, C. J., "Optical coherence tomography in Barrett's esophagus," *Gastrointest. Endosc. Clin. N. Am.* **23**(3), 549–563 (2013).
- [12] Ferrante, G., Presbitero, P., Whitbourn, R., and Barlis, P., "Current applications of optical coherence tomography for coronary intervention," (2013).
- [13] Abdolmanafi, A., Duong, L., Dahdah, N., and Cheriet, F., "Deep feature learning for automatic tissue classification of coronary artery using optical coherence tomography," *Biomed. Opt. Express* **8**(2), 1203 (2017).
- [14] Hariri, L. P., Liebmann, E. R., Marion, S. L., Hoyer, P. B., Davis, J. R., Brewer, M. A., and Barton, J. K., "Simultaneous optical coherence tomography and laser induced fluorescence imaging in rat model of ovarian carcinogenesis," *Cancer. Biol. Ther.* **10**(5), 438–447 (2010).
- [15] Wang, T., "An overview of optical coherence tomography for ovarian tissue imaging and characterization," *Wiley Interdiscip. Rev. Nanomed. Nanobiotechnol.* **7**(1), 1–16 (2015).
- [16] Drexler, W., Liu, M., Kumar, A., Kamali, T., Unterhuber, A., and Leitgeb, R. A., "Optical coherence tomography today: speed, contrast, and multimodality," *J. Biomed. Opt.* **19**(7), 071412 (2014).
- [17] Schmitt, J., "Optical Coherence Tomography (OCT): A Review," *IEEE J. Sel. Top. Quantum Electron.* **5**(4), 1205–1215 (1999).
- [18] Watanabe, Y., Takakura, K., Kurotani, R., Abe, H., Atanabe, Y. U. W., Akakura, K. E. I. T., and Urotani, R. E. K., "Optical coherence tomography imaging for analysis of follicular development in ovarian tissue," *App. Opt.* **54**(19), 6111 (2015).
- [19] Welge, W. A., DeMarco, A. T., Watson, J. M., Rice, P. S., Barton, J. K., and Kupinski, M. A., "Diagnostic potential of multimodal imaging of ovarian tissue using optical coherence tomography and second-harmonic generation microscopy," *J. Med. Imaging* **1** (2014).
- [20] Brewer, M. a., Utzinger, U., Barton, J. K., Hoyng, J. B., Kirkpatrick, N. D., Brands, W. R., Davis, J. R., Hunt, K., Stevens, S. J., and Gmitro, A. F., "Imaging of the ovary," *Technol. Cancer Res. Treat.* **3**(6), 617–627 (2004).
- [21] Pande, P., Shrestha, S., Park, J., Serafino, M. J., Gimenez-Conti, I., Brandon, J., Cheng, Y.-S., Applegate, B. E., and Jo, J. a., "Automated classification of optical coherence tomography images for the diagnosis of oral malignancy in the hamster cheek pouch," *J. Biomed. Opt.* **19**(8), 086022 (2014).
- [22] Gossage, K. W., Tkaczyk, T. S., Rodriguez, J. J., and Barton, J. K., "Texture analysis of optical coherence tomography images: feasibility for tissue classification," *J. Biomed. Opt.* **8**(3), 570–575 (2003).
- [23] Depeursinge, A., Foncubierta-Rodriguez, A., Van De Ville, D., and Müller, H., "Three-dimensional solid texture analysis in biomedical imaging: Review and opportunities," *Med. Imag. Anal.* **18**(1), 176–196 (2014).
- [24] St-Pierre, C., Madore, W.-J., De Montigny, E., Trudel, D., Boudoux, C., Godbout, N., Mes-Masson, A.-M., Rahimi, K., and Leblond, F., "Dimension reductSt-Pierre, C., Madore, W.-J., De Montigny, E., Trudel, D., Boudoux, C., Godbout, N., ... Leblond, F. (2017). Dimension reduction technique using a multilayered descriptor for high-precision classification of ovarian cancer tissue using optic," *J. Med. Imag.* **4**, 41306 (10 2017).
- [25] Venhuizen, F., van Ginneken, B., Liefers, B., van Grinsven, M., Fauser, S., Hoyng, C., Theelen, T., and Sánchez, C., "Robust total retina thickness segmentation in optical coherence tomography images using convolutional neural networks," *Biomed. Opt. Express* **8**(7) (2017).

- [26] Liu, G. S., Zhu, M. H., Kim, J., Raphael, P., Applegate, B. E., and Oghalai, J. S., "ELHnet: a convolutional neural network for classifying cochlear endolymphatic hydrops imaged with optical coherence tomography," *Biomed. Opt. Express* **8**(10), 4579 (2017).
- [27] Burgansky-Eliash, Z., Wollstein, G., Chu, T., Ramsey, J. D., Glymour, C., Noecker, R. J., Ishikawa, H., and Schuman, J. S., "Optical coherence tomography machine learning classifiers for glaucoma detection: a preliminary study," *Invest. Ophthalmol. Vis. Sci.* **46**(11), 4147–52 (2005).
- [28] Singh, A. S. G., Schmoll, T., and Leitgeb, R. a., "Segmentation of Doppler optical coherence tomography signatures using a support-vector machine," *Biomed. Opt. Express* **2**(5), 1328–1339 (2011).
- [29] Pham, D. L., Xu, C., and Prince, J. L., "Current Methods in Medical Image Segmentation," *Annu. Rev. Biomed. Eng.* **2**(1), 315–337 (2000).
- [30] Heimann, T. and Meinzer, H.-P., "Statistical shape models for 3D medical image segmentation: a review," *Med. Imag. Anal.* **13**(4), 543–63 (2009).
- [31] DeBuc, D. C., [*A Review of Algorithms for Segmentation of Retinal Image Data Using Optical Coherence Tomography*], INTECH Open Access Publisher (2011).
- [32] Kafieh, R., Rabbani, H., and Kermani, S., "A review of algorithms for segmentation of optical coherence tomography from retina," *J. Med. Signals Sens.* **3**(1), 45–60 (2013).
- [33] Brand, S., Ponerós, J. M., Bouma, B. E., Tearney, G. J., Compton, C. C., and Nishioka, N. S., "Optical coherence tomography in the gastrointestinal tract," (2000).
- [34] Haralick, R. M., "Statistical and structural approaches to texture," *Proc. IEEE* **67**(5), 786–804 (1979).
- [35] Gonzalez, R. and Woods, R., [*Digital image processing*] (2002).
- [36] Pal, N. R. and Pal, S. K., "A review on image segmentation techniques," *Pattern Recognit.* **26**(9), 1277–1294 (1993).
- [37] Yezzi, A., Tsai, A., and Willsky, A., "A statistical approach to snakes for bimodal and trimodal imagery," *Proceedings of the Seventh IEEE International Conference on Computer Vision* **2**, 898–90 (1999).
- [38] Alirezaie, J., Jernigan, M. E., and Nahmias, C., "Neural network-based segmentation of magnetic resonance images of the brain," *IEEE Trans. Nucl. Sci.* **44**(2), 194–198 (1997).
- [39] Wang, S., Zhu, W., and Liang, Z.-P., "ShapeDeformation: SVM Regression and Application to Medical Image Segmentation," *Proceedings Eighth IEEE International Conference on Computer Vision. ICCV 2001* **2**, 209–216 (2001).
- [40] Cheng, K.-S., Lin, J.-S., and Mao, C.-W., "The application of competitive hopfield neural network to medical image segmentation," *IEEE Trans. Med. Imag.* **15**(4), 560–567 (1996).
- [41] Ashburner, J. and Friston, K. J., [*Image Segmentation*], INTECH Open Access Publisher (2011).
- [42] Ford, Jr., L. R. and Fulkerson, D. R., "Maximal flow through a network," *Canad. J. Math.* **8**, 399–404 (1956).
- [43] Felzenszwalb, P. F. and Huttenlocher, D. P., "Efficient graph-based image segmentation," *Int. J. Comput. Vis.* **59**(2), 167–181 (2004).
- [44] Osher, S. and Sethian, J. A., "Fronts propagating with curvature-dependent speed: Algorithms based on Hamilton-Jacobi formulations," *J. Comput. Phys.* **79**(1), 12–49 (1988).
- [45] Mishra, A., Wong, A., Bizheva, K., and Clausi, D. A., "Intra-retinal layer segmentation in optical coherence tomography images," *Opt. Express* **17**(26), 23719–28 (2009).
- [46] Kass, M., Witkin, A., and Terzopoulos, D., "Snakes: Active contour models," *Int. J. Comput. Vis.* **1**(4), 321–331 (1988).
- [47] Ji, Z., Xia, Y., Sun, Q., Cao, G., and Chen, Q., "Active contours driven by local likelihood image fitting energy for image segmentation," *J. Inf. Sci.* **301**, 285–304 (2015).
- [48] Yazdanpanah, A., Hamarneh, G., Smith, B. R., and Sarunic, M. V., "Segmentation of intra-retinal layers from optical coherence tomography images using an active contour approach," *IEEE Trans. Med. Imag.* **30**(2), 484–496 (2011).
- [49] Maintz, J. B. and Viergever, M. A., "A survey of medical image registration," *Med. Imag. Anal.* **2**(1), 1–36 (1998).
- [50] Chakravarty, M. M., Sadikot, A. F., Germann, J., Bertrand, G., and Collins, D. L., "Towards a validation of atlas warping techniques," *Med. Imag. Anal.* **12**(6), 713–726 (2008).

- [51] Cootes, T., "Active Appearance Models," *IEEE Trans. Pattern Anal. Mach. Intell.* **23**(6), 681–685 (2001).
- [52] Wang, D. and Terman, D., "Locally Excitatory Globally Inhibitory Oscillator Networks," *IEEE Trans. Neural Netw. Learn. Syst.* **6**(1), 283–286 (1995).
- [53] Wang, D. L. and Terman, D., "Image segmentation based on oscillatory correlation," *Neural Comput.* **9**(4), 805–836 (1997).
- [54] Connolly, D. C., Bao, R., Nikitin, A. Y., Stephens, K. C., Poole, T. W., Hua, X., Harris, S. S., Vanderhyden, B. C., and Hamilton, T. C., "Female mice chimeric for expression of the simian virus 40 TAg under control of the MISIR promoter develop epithelial ovarian cancer," *Cancer Res.* **63**(6), 1389–1397 (2003).
- [55] Quinn, B. A., Xiao, F., Bickel, L., Martin, L., Hua, X., Klein-Szanto, A., and Connolly, D. C., "Development of a syngeneic mouse model of epithelial ovarian cancer," *J. Ovarian Res.* **3**(1), 24 (2010).
- [56] Romero-Aleshire, M. J., Diamond-Stanic, M. K., Hasty, A. H., Hoyer, P. B., and Brooks, H. L., "Loss of ovarian function in the VCD mouse-model of menopause leads to insulin resistance and a rapid progression into the metabolic syndrome," *Am. J. Physiol. Regul. Integr. Comp. Physiol.* **297**(3), 587–92 (2009).
- [57] Rasband, W., "ImageJ," *U. S. National Institutes of Health, Bethesda, Maryland, USA*, //imagej.nih.gov/ij/ (2012).
- [58] Schmitt, J. M., Xiang, S. H., and Yung, K. M., "Speckle in Optical Coherence Tomography," (1999).
- [59] Gossage, K. W., Smith, C. M., Kanter, E. M., Hariri, L. P., Stone, A. L., Rodriguez, J. J., Williams, S. K., and Barton, J. K., "Texture analysis of speckle in optical coherence tomography images of tissue phantoms," *Phys. Med. Biol.* **51**(6), 1563–1575 (2006).
- [60] Podoleanu, A. G., "Optical coherence tomography," *J. Microsc.* **247**(3), 209–219 (2012).
- [61] Roerdink, J. and Meijster, A., "The Watershed Transform: Definitions, Algorithms and Parallelization Strategies," *Fundam. Inform.* **41**(1-2), 187–228 (2000).
- [62] Jiang, J., Trundle, P., and Ren, J., "Medical image analysis with artificial neural networks," *Comput. Med. Imaging Graph.* **34**(8), 617–631 (2010).
- [63] Haralick, R., Shanmugan, K., and Dinstein, I., "Textural features for image classification," (1973).